ASPECTS OF THEORETICAL AND EXPERIMENTAL INVESTIGATIONS ON AIRFRAME/ENGINE INTEGRATION PROBLEMS

H. Hoheisel*, R. Kiock*, C.C. Rossow*,
A. Ronzheimer*, W. Baumert**, H. Capdevila*

Deutsche Forschungsanstalt für Luft- und Raumfahrt e.V. (DLR)
F. R. Germany

Abstract

In view of the development of ultra-high bypass engines, the aerodynamic interference between airframe and engine becomes more and more important. This study describes as a first step the flow field around an Airbus-type configuration with a conventional turbofan engine. Theroretically, the three-dimensional Euler equations were solved using a cell-vertex method using a multi-block structure. Experimentally, a half model based on the Airbus A320 and scaled about 1:10 with a Turbo-Powered Simulator was investigated at low speed. The results show good agreement between theory and experiment.

1. Purpose of Investigation

In aerodynamic design great interest is focussed on an optimal adaptation of propulsion system and airframe in order to achieve maximum efficiency from the mounted engine. This requires a careful investigation of the interference phenomena arising in the flow around a complete aircraft. Jet engine design tends to ultra-high bypass ratios which can be realized with lower specific fuel consumption. However, the large fan diameters required cause even stronger engine-airframe interaction. The aim of the presented contribution is directed to start investigations on ultra-high bypass engines. In view of interaction, acoustics and landing gear height, the shrouded fan appears more promising than the unshrouded one. Therefore, emphasis is laid on shrouded engines in this paper.

The fundamental importance of engine-airframe integration was emphasized during the AIAA 22nd Aerospace Sciences Meeting in 1984 by a special colloquium held on this topic. The twelve invited papers and five additional contributions were edited by S.N.B. Murthy and G.C. Paynter [1] and are viewed as a standard on computation of engine-airframe integration. S.N.B. Murthy stresses in his preface that "the rationalization of aerodynamic integration of an airplane in all aspects can be accomplished only on a hybrid analytical-experimental-computational basis". Experimental studies are seen to provide the basis for verification of outputs from numerical codes and have to be of very high quality.

Recent theoretical investigations applying potential flow equations on wing-body nacelle pylon configurations are known from E.N. Tinoco et al.[2], C. Haberland and G. Sauer[3](panel methods), Wang Dieqian and S.G. Hedman[4] (transonic small perturbation method) and A.W. Chen et al.[5] (full potential method). The more complex solution of the Euler equations was carried out for nacelle flows by S. Leicher et al.[6], R. Radespiel et al. [7] and N. Hirose et al.[8]. Experimental data were shown by the authors mentioned above in the cases of flight[2] and wind tunnel[2, 4, 5, 6, 8] and, moreover, by D. Eckert and W. Burgsmüller [9], W. P. Henderson [10] and O.C. Pendergraft Jr. et al.[11].

In the paper presented here the solution of the Euler equations will be used to predict interference phenomena between aircraft and engine. The advantage of the solution of the Euler equations with respect to the potential flow model is that the vortex sheet behind a lifting wing needs not to be specified. Furthermore the potential flow models do not allow entropy rise through shock waves while mass, momentum, and energy are conserved. On the other hand, compared to the solution of the Navier-Stokes equations the calculation of inviscid flow fields by solving the Euler equations tends to be an order of magnitude less expensive, and therefore as a first step in numerical simulation of interference effects here the application of an Euler code is preferred.

The special configuration considered here is a twin-engine Airbus-type aircraft. Dimensionless prarameters have to be defined in order to be able to compare the model investigation with the real aircraft. The flow around wing-body and engine was calculated by a numerical scheme for the solution of the Euler equations. Experiments were carried out on a half model with engine simulation by a Turbo-Powered Simulator at low speed. This investigation is to be seen as a first step for understanding the interference effects especially at low speed.

* Institut für Entwurfsaerodynamik, D-3300 Braunschweig

** Hauptabteilung Windkanäle, D-3400 Göttingen

2. Parameters of Engine Simulation

Each model investigation requires the consideration of similarity rules in order to be able to compare the flow field around the model and around the real aircraft. From general wind tunnel testing some parameters are known which are also of importance in case of engine simulation:

Mach number:

$$Ma_\infty = V_\infty / a_\infty \qquad (1)$$

Reynolds number:

$$Re_l = l_\mu V_\infty / \nu_\infty \qquad (2)$$

l_μ as a typical length of the model must not be too small in view of the required accuracy of the experiments.

Degree of turbulence:

$$Tu_\infty = 100 \sqrt{\overline{v'^2}} / V_\infty \qquad (3)$$

Special parameters for engine simulation are:

a) Kind of simulation: Jet engine simulation is carried out by simple representation of the nacelle geometry (trough flow nozzle) or by modelling of nacelle and jet. The best simulation can be achieved by a Turbo-Powered Simulator (TPS) which produces a stream tube upstream and downstream of the simulator. In this case, some more parameters have to be taken into account which describe the thrust (influence of jet downstream of engine) and the stream tube upstream of the engine (size of displacement).

b) The thrust coefficient is defined by net thrust of fan and turbine, wing area and dynamic pressure:

$$c_T = F_N / (A_W q_\infty) \qquad (4)$$

The different types of engines - low bypass and ultra-high bypass types - are better described by the following equation (see H. Grieb and D. Eckardt [12])

$$c_S = F_N / (A_\infty q_\infty) \qquad (5)$$

Between the two coefficients c_T and c_S the following connection is given:

$$c_S = c_T \cdot A_W / A_\infty \qquad (6)$$

c) The stream tube area ratio is given by the stream tube area far upstream and by the highlight area

$$\epsilon_{HL} = A_\infty / A_{HL} = (D_\infty / D_{HL})^2 \qquad (7)$$

However, it is not possible to realize the true bypass ratio because the turbine is driven by cold air in the wind tunnel. There the total temperature at turbine exit amounts only to 20 or 30% of that of the aircraft engine. This fact seems to be less severe since the fan jet is dominant in view of interference with the airframe.

3. Theoretical Investigation

Governing Equations

The three-dimensional Euler equations for unsteady compressible inviscid flows may be written in integral form using a cartesian coordinate system as

$$\iiint_V \frac{\partial}{\partial t} \vec{W} dV = - \iint_{\partial V} \vec{\vec{F}} \cdot \vec{n} \, dS, \qquad (8)$$

where

$$\vec{W} = \begin{bmatrix} \rho \\ \rho u \\ \rho v \\ \rho w \\ \rho E \end{bmatrix}, \quad \vec{\vec{F}} = \begin{bmatrix} \rho \vec{q} \\ \rho u \vec{q} + p \vec{i}_x \\ \rho v \vec{q} + p \vec{i}_y \\ \rho w \vec{q} + p \vec{i}_z \\ \rho H \vec{q} \end{bmatrix}$$

In equation (8), p, ρ, u, v, w, E and H are the pressure, density, cartesian velocity components, total energy and total enthalpy, respectively. V denotes an arbitrary control volume fixed in time and space and ∂V is the closed boundary of the volume. $\vec{\vec{F}}$ represents the tensor of flux density and $\vec{n}$ is the outward facing normal along ∂V. The unit vectors of the cartesian coordinate system are given by $\vec{i}_x$, $\vec{i}_y$, $\vec{i}_z$, and the velocity vector is hence

$$\vec{q} = u\vec{i}_x + v\vec{i}_y + w\vec{i}_z \, . \qquad (9)$$

Applying the integral mean value theorem, equation (8) can be converted to

$$\left(\frac{\partial}{\partial t} \vec{W} \right)^{av} = - \frac{\iint_{\partial V} \vec{\vec{F}} \cdot \vec{n} \, dS}{\iiint_V dV} \qquad (10)$$

The term on the left-hand side of equation (10) represents the integral mean value of the rate of change of $\vec{W}$ in the control volume V, and the right-hand side is the flux per volume of mass, momentum and energy through the surface of V. Together with the equation of state

$$p = \rho R T \qquad (11)$$

which relates the pressure to the components of $\vec{W}$, equation (10) forms a system of five equations for the unknowns ρ, u, v, w and E.

Solution Method

The discretization of equ. (10) follows the method of lines, i.e. the discretizations in space and time are done seperately. The physical domain around the aerodynamic body is divided into hexahedral cells by the generation of a body-fitted grid. The discrete values of the flow quantities are located at the cell vertices of the mesh cells, as proposed in [13]. The numerical analogue of the integral equation (10) then reads:

$$\frac{d}{dt}\ \vec{W}_{i,j,k} = \frac{1}{V_{i,j,k}}\left[\vec{Q}_{i,j,k} + D_{i,j,k}\right] \quad (12)$$

where i,j,k are the indices of a certain grid point in the computational domain, $\vec{Q}_{i,j,k}$ denotes the convective flux given by an approximation of the surface integration in equ. (10), and $\vec{D}_{i,j,k}$ is a dissipative operator.

The approximation of the convective flux at a vertex i,j,k is accomplished by first evaluating the fluxes through the surfaces of all cells surrounding node i,j,k. On regular 3-D body fitted grids a vertex has eight neighboring cells in common, shown in Figure 1. The surface integration is evaluated for each cell using an arithmetic average of the flux quantities at the vertices to determine the values on a cell face. Then the fluxes of all cells having node i,j,k in common are summed up to give $\vec{Q}_{i,j,k}$.

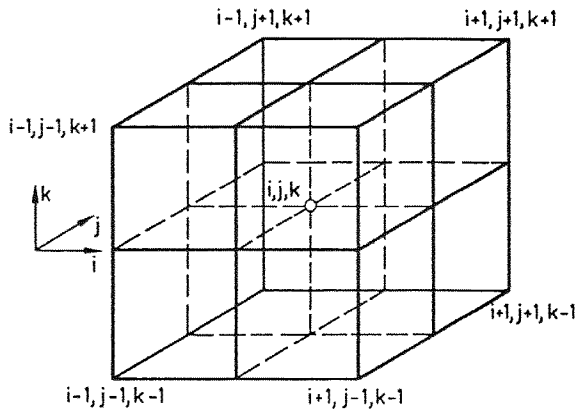

Fig. 1 Arrangement of cells in a regular three-dimensional mesh

As this discretization scheme leads to central difference approximations for the governing equations, additional artificial dissipative terms are necessary to damp out high frequency oscillations. Here a blend of second and fourth differences at the flow variables as described by A. Jameson et al. [14] is used to form the dissipative operator $\vec{D}_{i,j,k}$.

The spatial discretization results in a system of ordinary differential equations in time which is solved by an explicit 5-stage Runge Kutta time stepping scheme. Since interest is focussed on steady flow fields, various techniques, like local time-stepping, implicit residual averaging, and enthalpy damping [14], [15] are used to accelerate the convergence to the steady state.

In order to treat solid surface boundaries a flow tangency condition is enforced by projecting the velocity vector at a surface grid point onto the surface. Far field boundary conditions are implemented using the concept of characteristics variables described by D.L. Whitfield and J.M. Janus [16]. The specification of the engine operating conditions is done following R. Radespiel [17] by defining the stream tube area ratio and the pressure ratio p_{tj}/p_∞ and the temperature ratio T_{tj}/T_∞ at the engine outflow boundaries.

The algorithms are implemented in the DLR code CEVCATS. This code is written in a block-structured form which allows calculations with a nearly unrestricted number of grid points on arbitrary grid topologies. The details of the multiblock structure implemented in the program are found in reference [18].

Grid Generation

The approach of generating regular body-fitted, blockstructured meshes is employed. The use of regular body-fitted grids exploits the advantage of mapping the physical domain into a hexahedral computational domain, where the computational coordinates i,j,k may be taken as pointers for storage arrays leading to a well defined data structure. As it is not always possible to map the physical domain into a single computational block the physical domain is subdivided into a number of zones which are then separately mapped into computational blocks. Connectivity between the blocks is achieved via data transfer across corresponding block faces. This so-called multi-block approach allows a high flexibility for complex configurations. Using the multi-block approach one has at first to decide about a global grid topology which allows an embedding of necessary subgrids around the different components of a complex configuration. In the present work an H-O mesh topology was chosen for the global grid around the wing-body configuration. In this grid the H-type structure is employed in streamwise direction and the O-type structure in spanwise direction. In such a grid all aerodynamic surfaces will be represented by slits. Due to the H-topology a subblock in the global grid can easily be defined in order to allow an embedding of the grid around the engine.

For the grid around the engine also an H-type structure in streamwise direction is employed. The H-grid generated for a section of the engine may then be rotated to form a polar grid around the whole engine. This polar subgrid has to be fitted into the global grid.

In the present study the generation of field grids is established by the solution of an elliptic system of equations. Elliptic grid generation was mainly influenced by the work of J.F. Thompson et al. [19]. The present approach to elliptic grid generation is based on the work of T. Sonar and R. Radespiel [20]. However, it was found necessary to use a different concept for the control of grid properties:

The elliptic generation system commonly used is given by

$$\nabla\xi_i^2 = g^{ii}\, p_i \qquad i = 1,2,3 \qquad (13)$$

where ξ_i are the curvilinear coordinates, g^{ii} are the corresponding diagonal components of the covariant metric tensor, and p_i are the source terms necessary to control grid properties. As the source terms are not known a priori they have to be determined iteratively. In order to do so here at first a sheet of so-called target points is constructed. These target points define the desired position of all grid points closest to the boundaries of the domain. During the iterative solution process the deviation between target points and the actual position of the grid points is used to form an update of the source terms. This strategy resulted in a quite robust generation system, and together with a successive grid refinement strategy the generation of a global H-O grid around the wing-body configuration required only 6-7 minutes on a Cray XMP for a grid with about 240 000 mesh points.

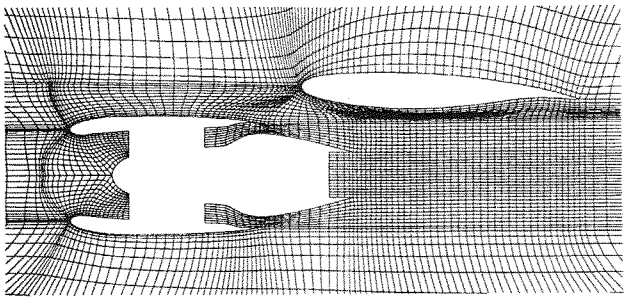

Fig. 2 View of grid section through engine and wing

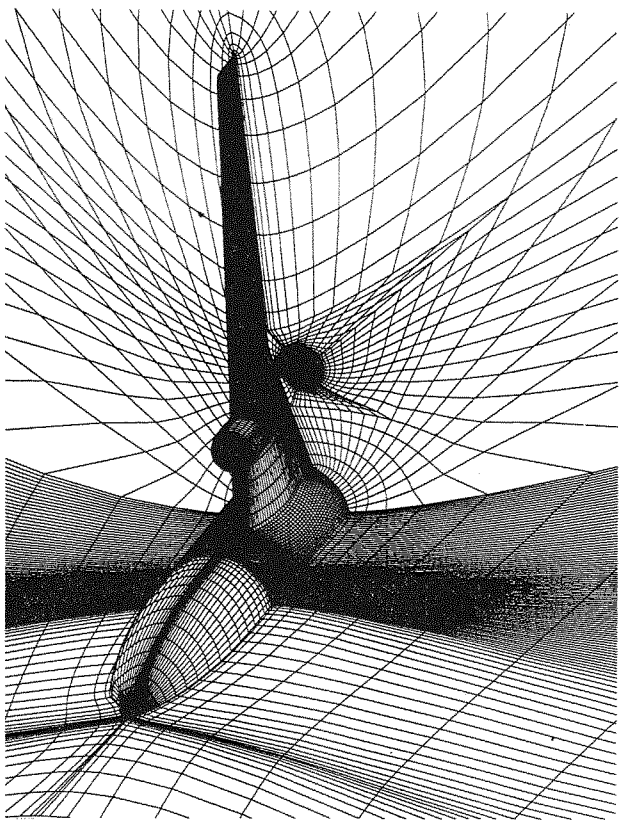

Fig. 3 Perspective view of complete grid around wing-body-engine, configuration

Figure 2 shows a section of the grid through engine and wing. In this work no attempt was made to generate a mesh around the pylon. Figure 3 gives a perspective view of the grid around the complete wing-body-engine configuration. It should be noted that at this stage of the work the fitting of the engine's subgrid into the global grid was achieved using only algebraic techniques rather than elliptic generation.

A detailed description of the elliptic grid generation system developped during this work may be found in [21].

4. Set-up of Experimental Investigations

Geometry of the Model

The investigations were carried out with a wind tunnel model in tail-off configuration as shown in Figure 4. This model named ALVAST is a half model to get relatively large dimensions for later investigations with flaps. It is designed following the Airbus A320 and scaled about 1:10 giving a half span width of b = 1.714 m and a reference wing chord of l_μ = 0.41 m.

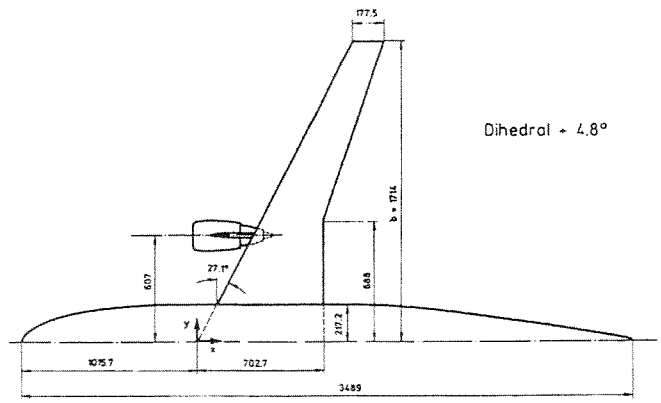

Fig. 4 ALVAST half model

The engine is modelled by a Turbo-Powered Simulator (TPS) of the type TDI 441 with a fan tip diameter of D_F = 127 mm and with an axisymmetric inlet, see Figure 5. Unfortunately, a simulator of true scale was not available for these experiments. With respect to CFM 56-5A1, the scale of the used simulator was about 1:13.

Typical parameters of this TPS are:

Fan-tip diameter	D_F = 127 mm (5")
Rotational speed	N = 45000 min^{-1}
Total pressure ratio	π_F = 1.55
Fan mass flow	$\dot{m}_F$ = 2.11 kg/s

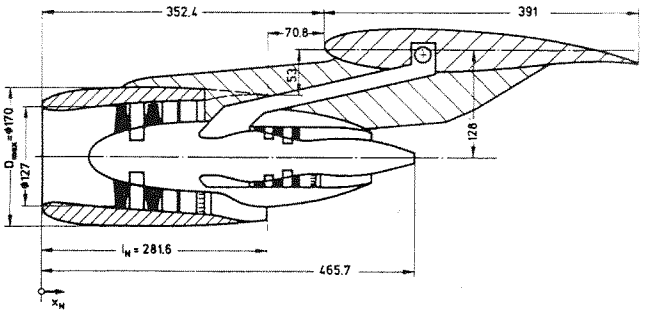

Fig. 5 Scetch of wing installed TPS

For a given speed of V_∞ = 60 m/s, the c_T of the TPS amounts only to 60% compared with that of CFM 56 due to incorrect scaling as mentioned above (Figure 6). The thrust coefficients calculated for the real engines namely the CRISP conception and the CFM 56 agree because these two engines have to fulfill the same purpose, i.e. to drive the A320 Airbus type. In the case of the stream tube area ratio, the TPS simulates well the one of the CFM 56 engine.

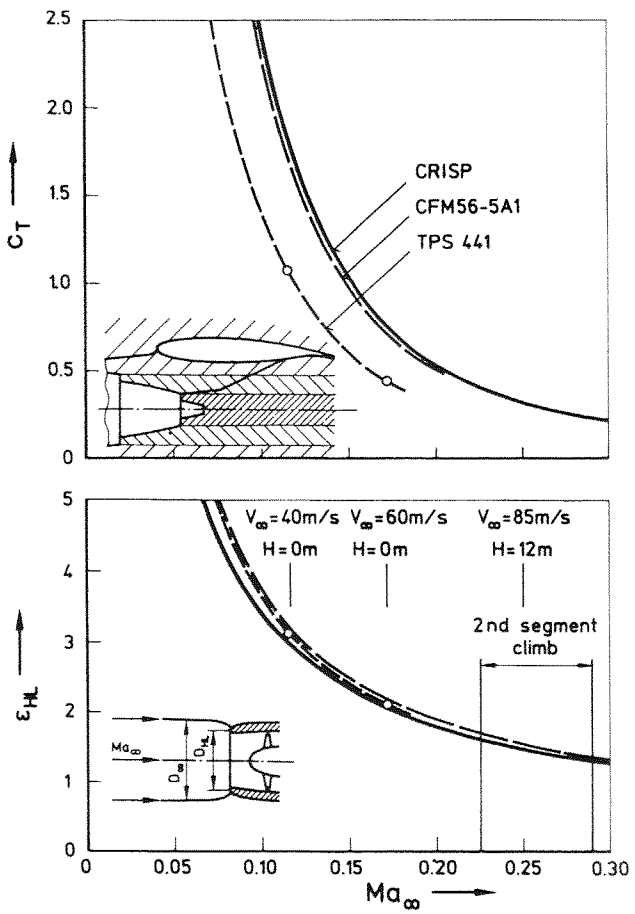

Fig. 6 Thrust coefficient and stream tube area ratio

Data Aquisition

The experimental investigations include

- the calibration of the TPS in the Calibration Tank Göttingen (ETG), see Baumert et al. [22]
- the test of the separate engine - pylon (EP) configuration in the Low-Speed Tunnel Göttingen (NWG)
- the test of the wing-body (WB) configuration in the NWG
- the test of the wing-body engine pylon (WBEP) configuration in the NWG

The measurements were performed mainly for a free-stream Mach number of Ma_∞ = 0.17 at different angles of attack and various thrust coefficients. This Mach number corresponds to a velocity of V_∞ = 60 m/s and to a wing Reynolds number of $Re_1 = 1.6 \cdot 10^6$ Some Measurements were also carried out at V_∞ = 40 m/s. Due to the limited tunnel speed of the NWG, it was not possible to run the tests in the second segment climb range, see Figure 6.

The degree of turbulence amounts to Tu = 0.3 %. The boundary layer transition was not influenced by any artificial tripping device.

Force and pressure distribution measurements were carried out during NWG testing. EP, WB or WBEP configuration was mounted on an external six-component balance. A large number of pressure taps was provided on the surfaces of wing, body and engine-nacelle and connected with a Scanivalve system (wing body) or with a PSI system (engine). More details are given by W. Baumert et al. [23].

The surface pressure of wing and nacelle is shown here by the pressure coefficient

$$c_p = (p - p_\infty)/q_\infty \qquad (14)$$

with

$$q_\infty = 0.5\ \rho_\infty V_\infty^2 \qquad (15)$$

The integration of the wing pressure coefficient determines the normal force coefficient of the wing section considered:

$$c_N = \int_{x/l} \Delta c_p d(x/l) \qquad (16)$$

Lift and drag coefficient are defined as usual:

$$c_L = L/(A_W q_\infty) \qquad (17)$$

$$c_D = D/(A_W q_\infty) \qquad (18)$$

Mass flow and rotational speed of the simulator were referred to standard conditions:

$$\dot{m}_{red} = \dot{m} \frac{p_{t,S}}{p_{t_\infty}} \sqrt{\frac{T_{t_\infty}}{T_{t,S}}} \qquad (19)$$

$$N_{red} = N \sqrt{\frac{T_{t,S}}{T_{t_\infty}}} \qquad (20)$$

with

$$p_{t,S} = 101\ 325\ \text{Pa}$$

$$T_{t,S} = 288{,}15\ \text{K}$$

The diameter of the stream tube far upstream of the engine is given by

$$D_\infty = \sqrt{\frac{4\dot{m}_F}{\pi V_\infty} \frac{RT_\infty}{p_\infty}} \qquad (21)$$

5. Results

Theoretical Results for Cruise and Take-off Conditions

The major part of the calculations presented in this paper was performed for the geometry of the ALVAST windtunnel model and a TPS representing the propulsion unit. The wing of the ALVAST-model was discretized using 30 cells in spanwise direction and 40 cells in chordwise direction on each the upper and lower side of the wing. The body was represented using 126 cells in streamwise direction and 36 cells in circumferential direction. 36 cells were placed chordwise on the outer nacelle and 42 cells in the same direction on the core engine. The rotation of the sectional engine grid was performed using 48 sections in circumferential direction. The far field was located about three wing spans away from the body. In total the number of grid points amounted to 375000, and 18 computational blocks were used.

The first calculation was performed for typical cruise conditions with an onflow Mach number of 0.75 and an angle of attack of 0.84°. The area ratio ϵ_{HL} for the nacelle inflow conditions was taken to 0.71.

No attempt was made to get a realistic simulation of the fan jet and the core jet at the engine outflow boundaries. The reason for this lies in the numerical viscosity inherent in the solution method. With the discretization scheme used here it is not possible to resolve the jump in velocity between jet and outer flow as a discontinuity. But the numerical dissipation, either introduced artificially or by the discretization scheme itself, forms a shear layer which has no physical meaning. Moreover, the formation of the shear layer will depend heavily on the grid resolution in this region, and certain interference effects may only be of purely numerical nature. In order to exclude such uncertainties no jet flow was modelled and an isentropic pressure ratio p_{tj}/p_∞ and a total temperature ratio T_{tj}/T_{t_∞} of unity were prescribed at the engine outflow planes.

It is worth to mention that this modelling has a small influence on the pressure distribution at the outer nacelle surface, as was already shown in [17].

In order to judge the interference effects caused by mounting an engine under the wing calculations were performed for either a wing body combination with and without engine. To allow a fair comparison the grid size of both configurations was identical, in essence the grid of the configuration without engine was the basic global mesh of the configuration with engine. This was done to remove uncertainties related to grid dependence of the solution as far as possible.

The pressure distributions obtained for these onflow conditions are shown in Figure 7, for the upper (left) and lower surface (right) of the wing. The solid lines are related to the wing-body-engine configuration (WBE) and the dashed lines correspond to the configuration without engine (WB). In this figure the sectional positions of the pressure distributions correspond to the spanwise location of grid points, however only every second distribution is shown to allow a more clear presentation. It can be seen from the figure that close to the root section of the wing the WBE configuration exhibits a stronger shock than WB alone. But further outboard the shock of WBE moves upstream and seems somewhat weaker than compared to WB.

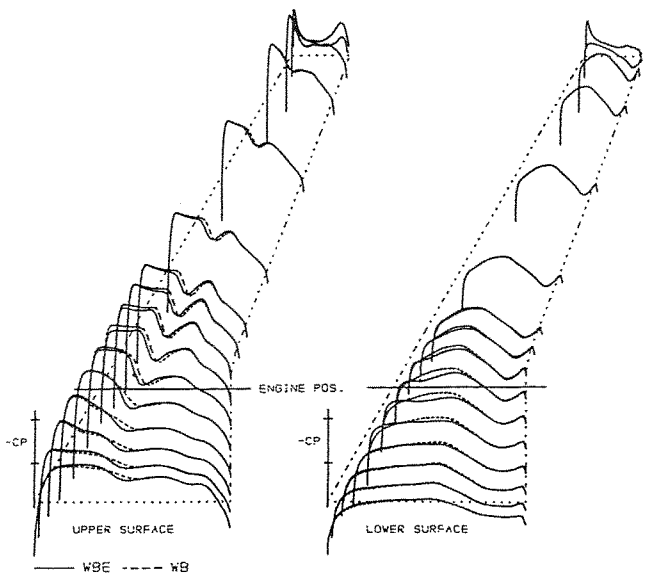

Fig. 7 Comparison of wing pressure distributions for wing-body (WB) and wing-body-engine configuration (WBE) at $Ma_\infty = 0.75$, $\alpha = 0.84°$, $\epsilon_{HL} = 0.71$

Figure 8 shows the spanwise lift distribution obtained for WBE and WB in this case. Surprisingly there is only a small

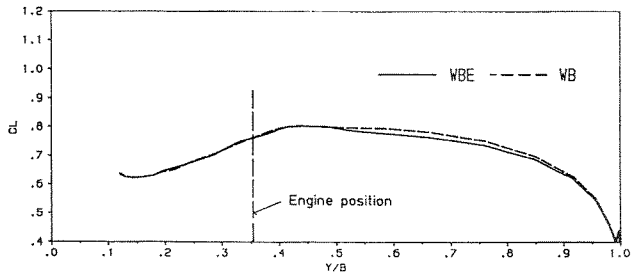

Fig. 8 Comparison of spanwise lift distribution for WB and WBE at $Ma_\infty = 0.75$, $\alpha = 0.84°$, $\epsilon_{HL} = 0.71$

deviation in regions of y/b > 0.5, i.e. not there where the engine is mounted but further outboard. This peculiar behaviour is better understood if one looks at the pressure distributions at four different spanwise sections, as given in Figure 9.

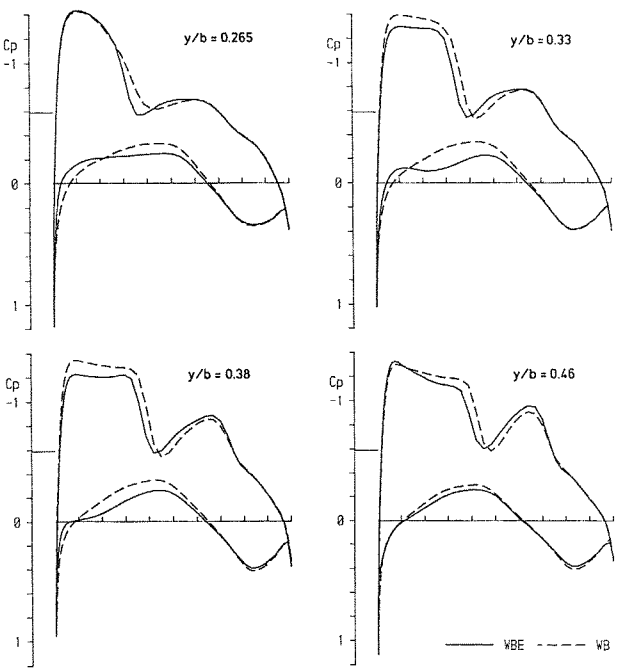

Fig. 9 Comparison of wing pressure distributions for WB and WBE at selected sections, at $Ma_\infty = 0.75$, $\alpha = 0.84°$, $\epsilon_{HL} = 0.71$

It can be seen that in the region where the engine is mounted (y/b = 0.354) the loss of lift due to the smaller supersonic region of WBE on the upper wing surface is compensated by the distribution on the lower surface, where the lowest pressure of WBE is always higher than that of WB. It has to be reminded that in the present investigation the pylon was not taken into account and therefore this behaviour may occur. Figure 10 gives a contour plot of lines of constant Mach number for a

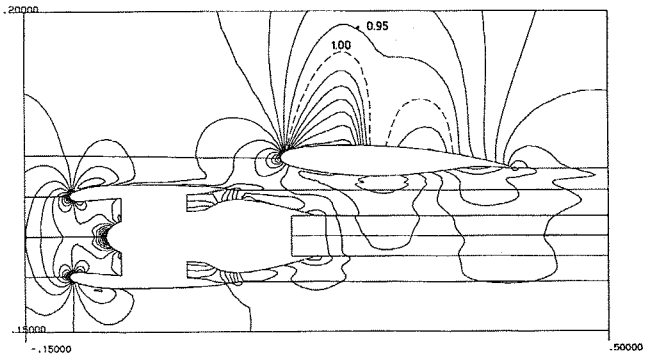

Fig. 10 Lines of constant Mach number for WBE at $Ma_\infty = 0.75$, $\alpha = 0.84°$, $\epsilon_{HL} = 0.71$

streamwise section of wing and engine. The broken curves indicate lines of Ma = 1, and the increment was chosen to $\Delta Ma = 0.05$. One clearly sees that no jet was modelled.

The next calculation was performed for subsonic flow conditions with an onflow Mach number of 0.171 and an angle of attack of 6.9°. The area ratio for the fan inflow conditions was $\epsilon_{HL} = 2.11$. These flow conditions may occur during take-off. Figure 11 shows the sectionwise pressure distributions in the same way as done for the cruise conditions. It is interesting to note that in the region between engine and body close to the root section the suction peaks on the upper surface are higher for the WBE configuration than

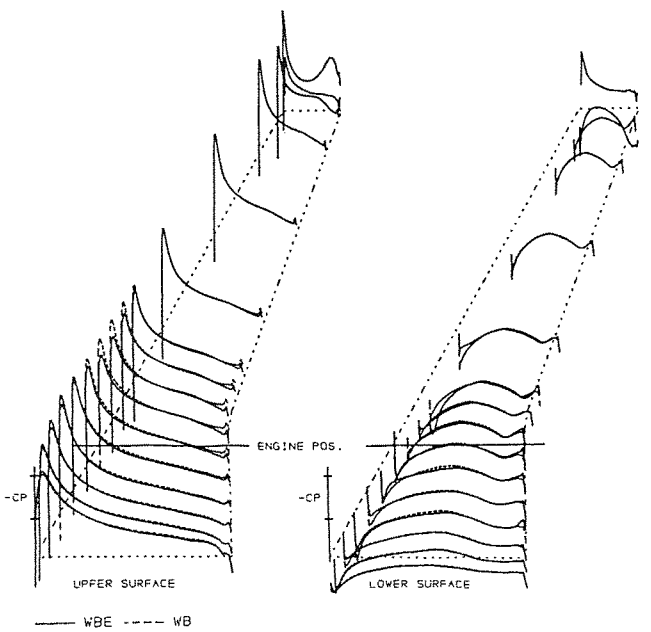

Fig. 11 Comparison of wing pressure distributions for WB and WBE at $Ma_\infty = 0.17$, $\alpha = 6.9°$, $\epsilon_{HL} = 2.11$

those of WB. This may be caused by a local acceleration of the flow due to displacement effects of body and engine. However, in the vicinity of the engine the suction peaks of WBE are significantly reduced compared to WB.

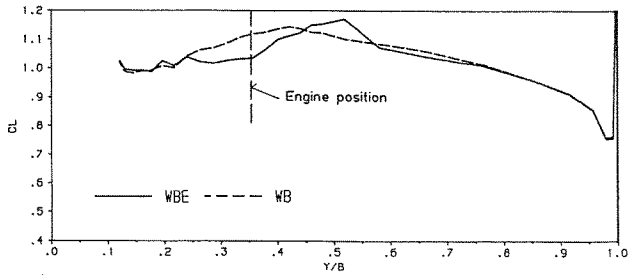

Fig. 12 Comparison of spanwise lift distribution for WB and WBE at $Ma_\infty = 0.17$, $\alpha = 6.9°$, $\epsilon_{HL} = 2.11$

Figure 12 shows the spanwise lift distribution. The c_L values of WBE are always lower than those of WB except between y/b = 0.45 and 0.55. This may be caused by the singular lines in the mesh which occur due to the embedding of the engine's subgrid into the global mesh. In the case of transonic flow this grid irregularities

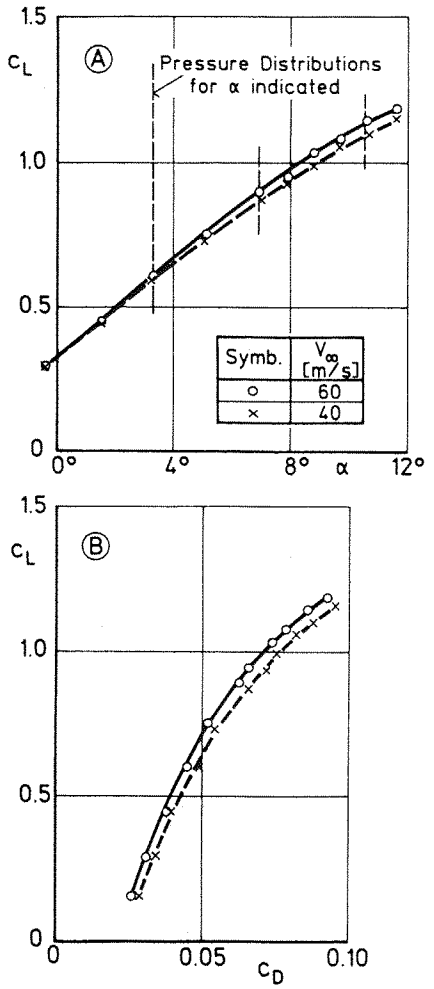

Fig. 13 Lift and drag coefficient for WB from experiments

had no influence on the solution, but when calculating such low Mach number flows the damping properties of the solution scheme are heavily degraded and local oscillations can occur. A remedy for this may be a higher concentration of grid points in that region and further more an elliptic mesh generation procedure for the embedding of the subgrid of the nacelle in order to control the grid spacing properly.

However, even for this case a converged solution was obtained within 600 time steps. This amounted to about 2.5 hours CPU time on a Cray XMP for WBE. For the transonic flow case only 400 time steps were necessary to drop the residual in all blocks by about three orders of magnitude.

Experimental Results for Take-off Conditions

Wing Pressure Distribution

The influence of the engine on the pressure distribution of the wing shall be considered on some lift-coefficients. To judge the wing behaviour on lift and drag Figure 13 shows c_L and c_D for the WB-configuration for two velocities V_∞. Reducing the upstream velocity V_∞ leads to higher drag as a result of the lower Reynolds number (8 to 10%).

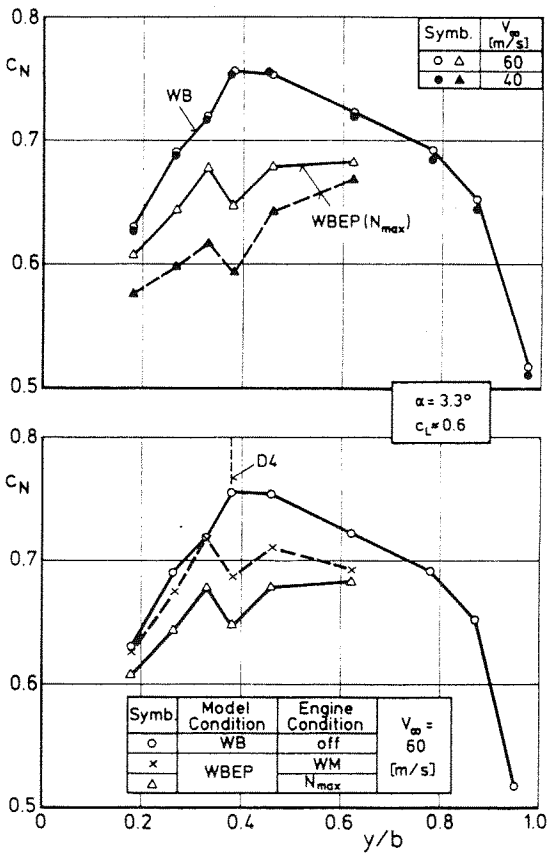

Fig. 14 Influence of engine condition on normal force coefficient from experiments

The interference effects caused by the engine will be demonstrated on results of the wing pressure distribution. For a lift coefficient of $c_L = 0.6$ ($\alpha = 3.3°$) Figure 14 shows the normal force coefficient c_N as the result of the integrated wing pressure distribution (see Figure 19) at different sections of the wing. The results in the lower diagram are given for two different engine conditions (wind milling WM and maximum rotational speed N_{max}) in comparison with the distribution of the WB configuration. In both cases (WM and N_{max}) the main influence of the engine on the force coefficient c_N is given at position y/b = 0.38 that means at the outboard side of the pylon, section D4.

Changing the thrust coefficient of an engine simulator there are different possibilities, namely by the thrust or by the dynamic pressure q_∞, see equation (4). Here the thrust was changed by changing the rotational speed at constant dynamic pressure. It should be noted that there is a coupling between the thrust coefficient c_T and the stream tube area ratio ϵ_{HL} which cannot be demonstrated independently by the experiments.

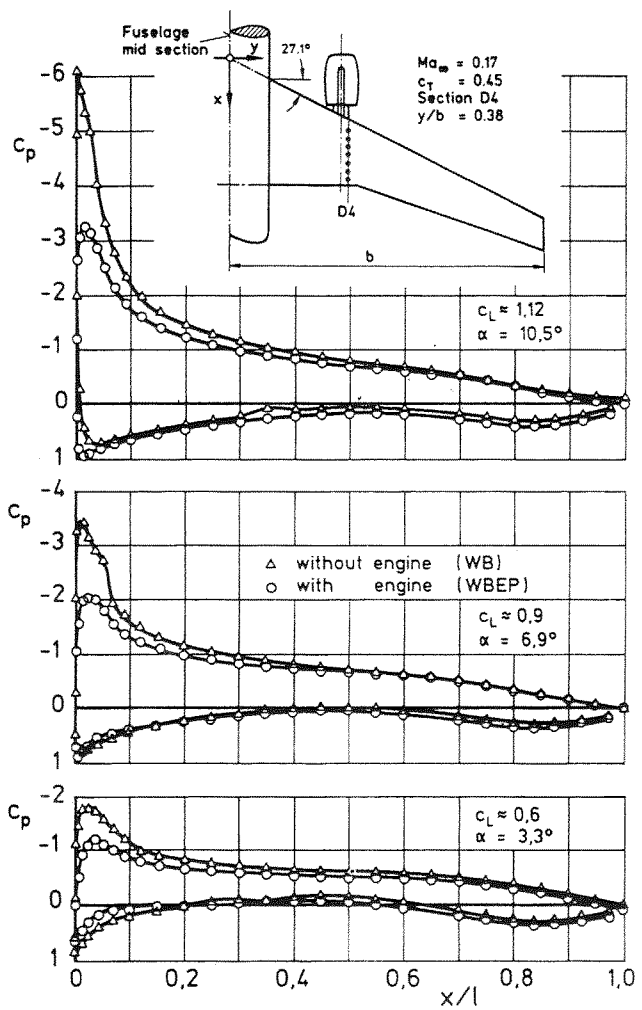

Fig. 15 Influence of engine simulation on wing pressure distribution from experiments

The second possibility of changing the engine thrust coefficient is demonstrated in the upper diagram of Figure 14. For the WB configuration no influence of the Reynolds number on the c_N distribution is shown at different upstream velocities V_∞. But for the WBEP configuration, the lower velocity V_∞ leads very clearly to a stronger engine influence by increasing the thrust coefficient from $c_T = 0.45$ to $c_T = 1.1$, see Figure 6 by changing the reference velocity V_∞.

The influence of the engine interference on the wing pressure distribution of the most important section D4 at different angles of attack is demonstrated in Figure 15, here for the thrust coefficient $c_T = 0.45$ (N_{max}). The engine effect does not change compared to the results before, i. e. the engine interference effects remain on the leading edge region of the wing at different angles of attack. In the complete α range the reduction of the normal force coefficient caused by the engine is nearly constant, see Figure 16.

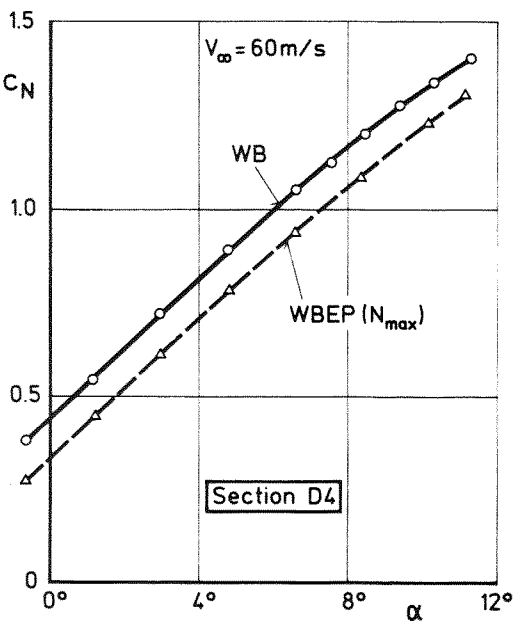

Fig. 16 Influence of engine simulation on normal force coefficient from experiments

Nacelle Pressure Distribution

Figure 17 allows the comparison of the EP and the WBEP configuration at N_{max}, $\alpha = 0°$. The fuselage displaces the flow and causes a 0.07 lower c_p at WBEP compared with EP (outside front region, $\varphi = 60°$ and 180°). At $\varphi = 300°$ the c_p values agree: the displacement effect of the fuselage is compensated by a certain "blockage" in the "corner" between wing and nacelle. The rear part of the outer nacelle pressure is also influenced by fuselage and wing, in parparticular at $\varphi = 300°$. Here the nearby wing dominates due to sweep and dihedral at this location, in contrast to $\varphi = 60°$.

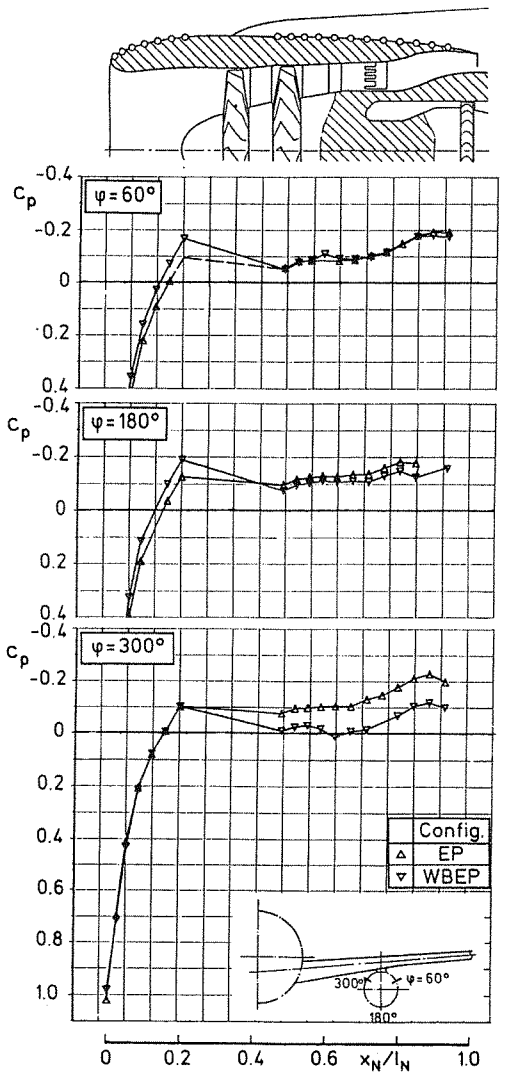

Fig. 17 Measured nacelle pressure distribution, N_{max}, V_∞ = 60 m/s, a = 0°

From extensive testing, the location of the nacelle stagnation point was evaluated and plotted in Figure 18. The stagnation point moves linear along the surface coordinate outward with increasing rotational speed, stream tube area ratio and thrust coefficient (upper diagram). It also varies linear with the angle of attack depending on the circumferential location (lower diagram). The results of EP and WBEP configuration agree with respect to the accuracy of the stagnation point evaluation.

Further, it is assumed that the wing causes a deviation of the streamlines in the region of the nacelle. This local angle of attack cannot be analyzed with these experimental data.

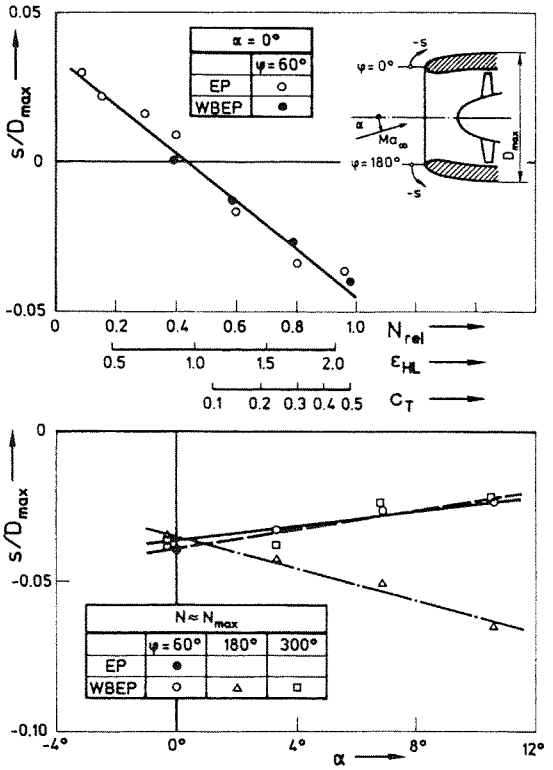

Fig. 18 Location of nacelle stagnation point, V_∞ = 60 m/s, from experiments

Comparison of Theoretical and Experimental Results

As test case for the comparison of theoretical and experimental results the onflow conditions Ma_∞ = 0.171 and α = 3.3° are used. A constant thrust coefficient of c_T = 0.45 was achieved at a rotational speed of N_{max} in the experimental investigation, for the theoretical simulation ε_{HL} = 2.11 was prescribed at fan inflow. In the left hand part of Figure 19 the pressure distribution at the four sections obtained by the measurements is given. The interference effect caused by the engine can clearly be seen in the reduction of the suction peak at the leading edge. Particularly section D4, i.e. the first outboard section next to the pylon, shows a reduction of the suction peak by Δc_p = 0.65.

The right part of Figure 19 shows that the calculated pressure distributions of the configuration without engine correspond quite well to the measured pressure distributions of the clean configuration. The calculated minimum pressure coefficients in all sections are Δc_p = 0.2 higher than the measured values. Looking at the configuration with engine, the interference effects caused by the engine seem somewhat underpredicted compared to the experimental results. This may be mainly caused by two reasons: First, the calculations do not take into account the pylon.

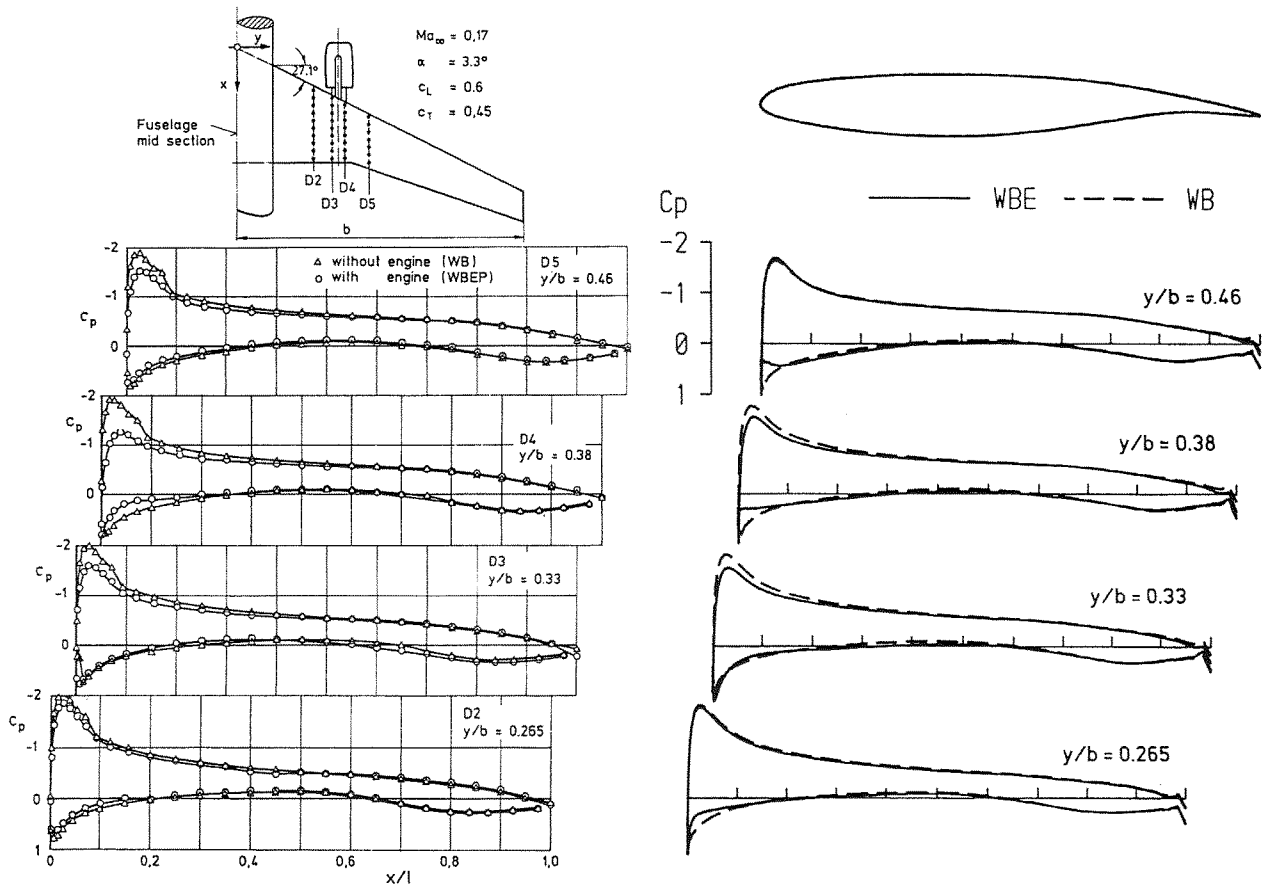

Fig. 19 Comparison of wing pressure distributions, calculation and experiment

The displacement effect of the pylon together with viscous effects at the junctions engine-pylon-wing may cause interference phenomena which are not accounted for in the calculation. Second, the interference effects probably caused by the jets of fan and core engine are not considered. Due to the fact that in this study only the inviscid flow field has been calculated the entrainment effect of the jet could not be simulated. However, the main engine effects are well described by the theory.

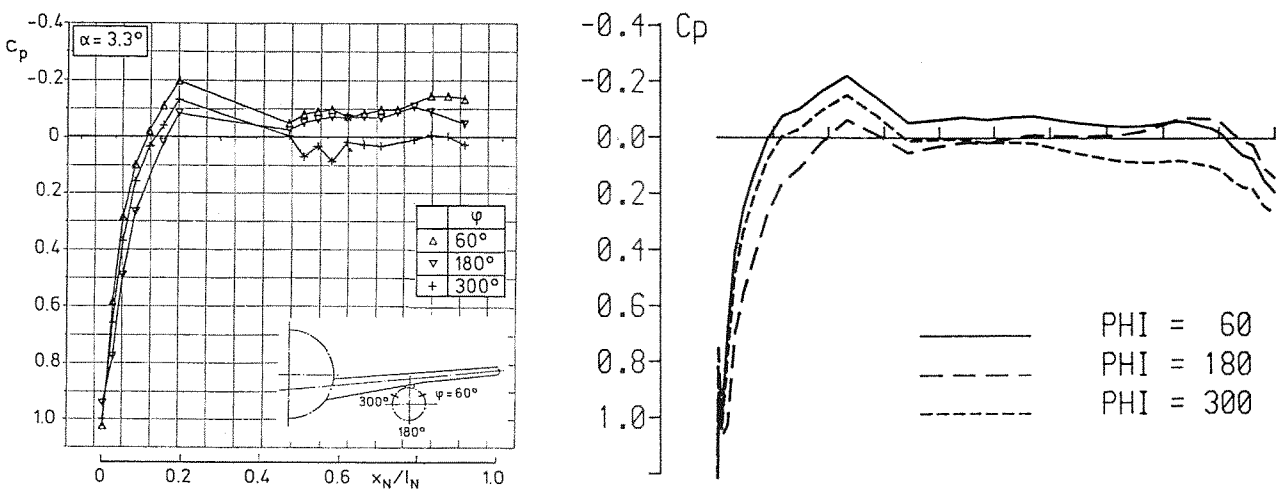

Fig. 20 Comparison of nacelle pressure distributions, calculation and experiment

Simulating only an inviscid jet by a non-isentropic pressure ratio p_{tj}/p_∞ will have no effect on the wing pressure distribution as long as the jet does not touch the wing and it is almost aligned with the mean flow direction. This was confirmed by numerical studies performed in parallel to this work. Therefore, in order to avoid effects of a numerically generated shear layer, only an isentropic pressure ratio was prescribed at the outflow boundaries of the engine, and no interference effects of the jet are modelled.

A further comparison of measured and calculated results was performed for pressure distributions at different circumferential sections of the nacelle. The left part of Figure 20 shows the experimental results, and the right part the theoretical data. The asymmetrical behaviour of the pressure distribution at $\varphi = 60°$ and 300° was discussed at Figure 17 already. The same tendency can be found in the calculated pressure distributions. Unfortunately, there are no tappings in the range of the suction peak found theoretically. Therefore, the results at $x_N/l_N = 0.19$ may be compared. The calculated values lie only $\Delta c_p = 0.03$ over the measured ones at $\varphi = 60°$ and 300°, the deviation amounts to $\Delta c_p = 0.10$ at $\varphi = 180°$. Furthermore, the slopes of the pressure distributions at the different angles show the same behaviour as in the experiment. Only at the trailing edge of the nacelle the calculated results tend to higher pressures due to the missing viscid jet modelling. But besides that deviation the agreement between measured and calculated data is excellent.

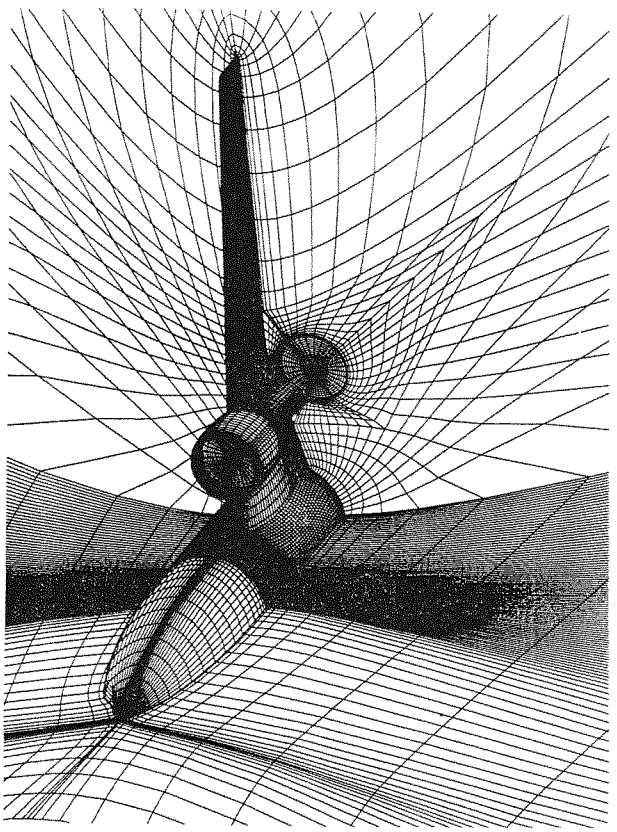

Fig. 21 Perspective view of grid around configuration of wing body and ultra-high bypass engine

These results confirm that some interference effects are correctly simulated already by the calculations of the inviscid flow field as done in the present study.

6. Conclusions

The interference of airframe and engine was studied theoretically and experimentally on an Airbus-type configuration. The three-dimensional Euler equations were solved by a cell vertex method using a body-fitted grid. The flowfield around the complex geometry of body, wing and engine was discretized with a block structured mesh. The engine operating conditions were specified by the stream tube ratio of the fan flow and by an isentropic pressure ratio p_{tj}/p_∞ and the temperature ratio $T_{tj}/T_{t\infty} = 1$ at the engine outflow boundaries. Pressure distributions on wing and nacelle were computed at both cruise and take-off flight conditions.

The experimental investigations concerned a half model based on the Airbus A320 and scaled about 1:10 with a Turbo-Powered Simulator at low speed. The main results may be summarized as follows:

1. At cruise condition, the computed pressure distribution shows a stronger shock close to the wing root section for the wing-body engine configuration (WBE) than for the wing-body configuration (WB) alone. The spanwise lift distributions look very similar because upper and lower side deficiencies compensate each other.

2. At take-off condition, the suction peak is higher at the wing root and lower in the engine region when WBE is compared with WB. The surprising higher local lift coefficient near the engine may be caused by singular mesh lines and corresponding damping problems at low speed.

3. Experiments at low speed show a clear reduction of the normal force coefficient due to the engine. This effect is strengthened with increasing thrust coefficient of the engine. This holds for the complete range of angle of attack considered here, $\alpha = 0°$ to 12°.

4. The calculated and the measured wing pressure distribution agree fairly well except in the wing front region. At suction peak, the calculated pressure coefficient is slightly higher at the

WB configuration compared with the measured one, but by the same amount lower at the WBE configuration at two stations each inboard and outboard of the engine. This may be caused by the facts that the calculation does not include pylon, jet and flow viscosity.

5. The calculated and the measured nacelle pressure distributions agree even better than those of the wing.

Since the development of jet engines tends towards ultra-high bypass ratios, the next step will be the theoretical and experimental investigation of the interference of the existing model with an UHB engine. Figure 21 shows the grid of such a configuraton. Due to the considerable bigger nacelle diameter, stronger interference effects are expected. The optimum geometric arrangement has to be determined in view of the direct operating costs of such an airplane.

References

[1] Murthy, S.N.B.; Paynter, G.C.; (editors): Numerical Methods for Engine-Airframe Integration. Progress in Astronautics and Aeronautics, Vol. 102. AIAA New York (1986).

[2] Tinoco, E.N.; Ball, D.N.; Rice II, F.A.: PAN AIR Analysis of a Transport High-Lift Configuration. J. Aircraft Vol. 24, No. 3 (1987).

[3] Haberland, C.; Sauer, G.: On the Computation of Wing Lift Interference Caused by High Bypass Engines. ICAS-86-3.9.1 (1986).

[4] Wang, Dieqian; Hedman, S.G.: The Embedded Grid-Concept and TSP Methods Applied to the Calculation of Transonic Flow about Wing/Body/Nacelle/Pylon-Configurations. ICAS-88-4.7.2 (1988).

[5] Chen, A.W.; Curtin, M.M.; Carlson, R.B.; Tinoco, E.N.: TRANAIR Applications to Engine/Airframe Integration. AIAA-89-2165 (1989).

[6] Leicher, S.; Lücking, P.; Wehlitz, P.: Calculation of Flow Along a Cowl of a Shrouded Propfan Using a 3D-Euler Code. ICAS-88-5.1.4 (1988).

[7] Radespiel, R.; Horstmann, K.H.; Redeker, G.: Feasibility Study on the Design of a Laminar Flow Nacelle. AIAA-89-0640 (1989).

[8] Hirose, N.; Asai, K.; Ikawa, K.; Kawamura, R.: 3-D Euler Flow Analysis of Fanjet Engine and Turbine Powered Simulator with Experimental Comparison in Transonic Speed. AIAA-89-1835 (1989).

[9] Eckert, D.; Burgsmüller, W.: Simulation und Messung von Triebwerkseinflüssen an einem zweistrahligen Flugzeugmodell mit Hilfe von Modelltriebwerken. DGLR 85-92 (1985).

[10] Henderson, W.P.: Propulsion-Airframe Integration for Commercial and Military Aircraft. SAE-872411 (1987).

[11] Pendergraft, O.C., Jr.; Ingraldi, A.M.; Re, R.J.; Karija, T.T.: Nacelle/Pylon Interference Study on a 1/17th-Scale, Twin-Engine, Low-Wing Transport Model. AIAA-89-2480 (1989).

[12] Grieb, H.; Eckardt, D.: Propfan and Turbofan - Antagonism or Synthesis. ICAS-86-3.8.2 (1986).

[13] Rossow, C.-C.: Berechnung von Strömungsfeldern durch Lösung der Euler-Gleichungen mit einer erweiterten Finite-Volumen Diskretisierungsmethode. DLR-FB 89-38 (1989).

[14] Jameson, A.; Schmidt, W.; Turkel, E.: Numerical Solution of the Euler Equations by Finite Volume Methods Using Runge Kutta Time Stepping Schemes. AIAA 81-1259 (1981).

[15] Jameson, A.; Baker, T.J.: Solutions of the Euler Equations for Complex Configurations. AIAA 83-1929 (1983).

[16] Whitfield, D.L.; Janus, J.M.: Three-Dimensional Unsteady Euler Equations Solution Using Flux Vector Splitting. AIAA 84-1552 (1984).

[17] Radespiel, R.: Calculation of the Flow around Powered High Bypass Ratio Nacelles Using an Euler Code. DFVLR IB 129-87/25 (1987).

[18] Radespiel, R.; Kroll, N.: Progress in the Development of an Efficient Finite Volume Code for the Three-Dimensional Euler Equations. DFVLR-FB 85-31 (1985).

[19] Thompson, J.F.; Warsi, Z.U.A.; Mastin, C.W.: Numerical Grid Generation. North-Holland New York (1985).

[20] Sonar, T.; Radespiel, R.: Geometric Modelling of Complex Aerodynamic Surfaces and Three-Dimensional Grid Generation. In: Numerical Grid Generation in Computational Fluid Mechanics '88. Edited by S. Sengupta et al. Pineridge Press Limited, Swansea, UK (1988).

[21] Rossow, C.-C.; Ronzheimer, A.; Capdevila, H.: A Grid Generation Package for Wing-Body-Engine Configuration. DLR IB 129-90/15 (1990).

[22] Baumert, W.; Binder, B.; Stäger, W.: Engine Simulator Tests: Comparison of Calibration and Wind Tunnel Results. AGARD CP-429 pp. 25-1 to 25-11 (1987).

[23] Baumert, W. et al.: Der 3-m x 3-m-Niedergeschwindigkeits-Windkanal (NWG) der DFVLR in Göttingen (Stand 1988). DFVLR-Mitt. 89-05 (1989).